

SCIENTIFIC REPORTS

OPEN

Polymorphism Control of Layered MoTe₂ through Two-Dimensional Solid-Phase Crystallization

Jyun-Hong Huang¹, Hao-Hua Hsu¹, Ding Wang², Wei-Ting Lin², Chun-Cheng Cheng², Yao-Jen Lee^{3,4} & Tuo-Hung Hou¹ 

Two-dimensional (2D) molybdenum ditelluride (MoTe₂) exhibits an intriguing polymorphic nature, showing stable semiconducting 2H and metallic 1T' phases at room temperature. Polymorphism in MoTe₂ presents new opportunities in developing phase-change memory, high-performance transistors, and spintronic devices. However, it also poses challenges in synthesizing homogeneous MoTe₂ with a precisely controlled phase. Recently, a new yet simple method using sputtering and 2D solid-phase crystallization (SPC) is proposed for synthesizing high-quality and large-area MoTe₂. This study investigates the polymorphism control of MoTe₂ synthesis using 2D SPC. The Te/Mo ratio and oxygen content in the as-sputtered films correlate strongly with the final phase and electrical properties of SPC MoTe₂. Furthermore, the SPC thermal budget may be exploited for stabilizing a deterministic phase. The comprehensive experiments presented in this work demonstrate the versatile and precise controllability on the MoTe₂ phase by using the simple 2D SPC technique.

Two-dimensional (2D) molybdenum ditelluride (MoTe₂) shows a moderate bandgap close to that of Si¹, high carrier mobility^{2,3}, and a large spin-orbit coupling splitting in the valence band⁴. These unique properties are being explored for various electronics⁵⁻⁷, optoelectronics⁸, and spintronics^{9,10} applications. In contrast to most 2D transition metal dichalcogenides (TMDs) with only one monotonous phase stable at room temperature, 2D MoTe₂ exhibits intriguing polymorphism with a low phase transition barrier¹¹, and it can be directly synthesized into either a semiconducting or metallic phase^{5,12-14}. In the semiconducting 2H phase, the Mo and Te atoms are arranged in in-plane hexagonal symmetry and out-of-plane trigonal prismatic coordination with a space group of P6m2. In the metallic 1T' phase, they are arranged in in-plane monoclinic symmetry and out-of-plane octahedral coordination with a space group of P12₁/m1^{15,16}. Both 2H and 1T' phases not only are stable at room temperature, but also show robust thermal stability up to 815 and 900 °C, respectively¹⁷. Chemical vapor transportation (CVT)² is a popular method for synthesizing both 2H- and 1T'-MoTe₂ bulk materials by recrystallizing mixed Mo and Te powders at high temperatures (1100 °C for tens of hours). The cooling rate of the sample determines the final stable phase to be 2H or 1T'. The transition between 2H and 1T' phases after synthesis could be facilitated by supplying external energy through photons⁶, electrons¹⁸ and strains¹⁹. The ability of phase transition was recently explored for forming a lateral 1T'/2H heterophase junction in field-effect transistors (FETs) where the source/drain regions are selectively transformed into the 1T' phase to reduce the contact resistance^{6,20}. However, synthesizing high-quality 2D MoTe₂ with a controllable phase directly on large-area substrates remains extremely challenging by using conventional chemical vapor deposition (CVD). This is attributed to the weak bonding energy between Mo and Te atoms⁵, and also the aforementioned low transition barrier between the 1T' and 2H phases. The process window of CVD, depending on the CVD catalyst²¹, Te partial pressure^{12,13,22}, Mo precursors⁵, and turbulent flow control²³, is limited for MoTe₂, compared with that for other widely available TMDs such as MoS₂, MoSe₂, WS₂, and WSe₂. The lack of a reliable large-area synthesis process greatly hinders the practical use of MoTe₂.

Recently we demonstrated a new yet simple synthesis route for large-area, high-quality layered MoTe₂ by using a sputtering deposition followed by solid-phase crystallization (SPC)²⁴. The Mo and Te elements were directly supplied from a compound sputter target without complex chemical reactions and reactant transferring. Because

¹Department of Electronics Engineering and Institute of Electronics, National Chiao Tung University, Hsinchu, 300, Taiwan. ²Advanced Technology Research Center, AU Optronics Corporation, Hsinchu, 300, Taiwan. ³National Nano Device Laboratories, Hsinchu, 300, Taiwan. ⁴Department of Physics, National Chung Hsing University, Taichung, 402, Taiwan. Correspondence and requests for materials should be addressed to T.-H.H. (email: thhou@mail.nctu.edu.tw)

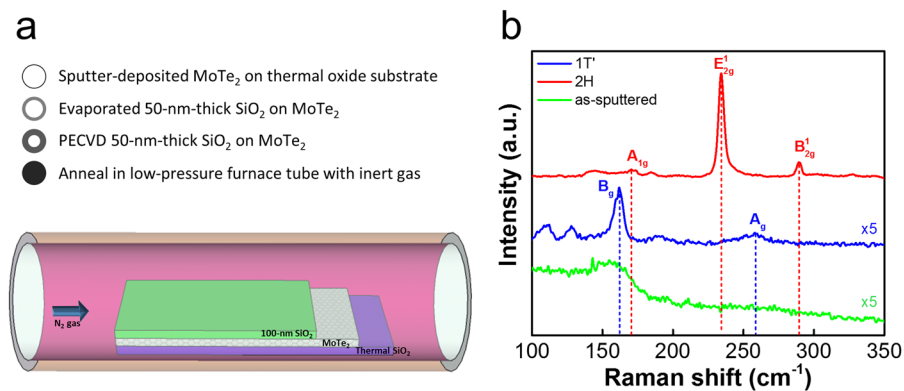


Figure 1. (a) SPC synthesis flow of large-area, high-quality $MoTe_2$, and (b) Raman spectra of as-sputtered $MoTe_2$, 2H- $MoTe_2$ SPC at 650 °C for 24 h, and 1T'- $MoTe_2$ SPC at 850 °C for 1 h.

of the physical bombardment of sputtering, the clustering of Mo and Te elements was random, and SPC was necessary to transform as-sputtered amorphous $MoTe_2$ thin films into layered structures. To prevent oxidation and decomposition of $MoTe_2$ during SPC at high temperatures, the as-sputtered $MoTe_2$ was first encapsulated using a SiO_2 capping layer before SPC, and SPC can be performed easily in a Te-free atmosphere. More comprehensive discussion on the SPC mechanism and electrical characteristics can be found in ref.²⁴. We also found that synthesizing homogeneous 1T'- and 2H- $MoTe_2$ is possible by controlling the SPC dwell time²⁴. However, the polymorphism control of SPC $MoTe_2$ is scientifically interesting and requires more comprehensive investigations.

In this work, the polymorphic SPC of $MoTe_2$ is studied depending on the composition of the as-sputtered $MoTe_2$ and the SPC thermal budget. The composition of the as-sputtered $MoTe_2$ was verified using X-ray photoelectron spectroscopy (XPS), and it was found that the composition can be modulated by varying the sputtering temperatures while using an identical $MoTe_2$ sputter target. $MoTe_2$ is known to be prone to oxidation^{17,25}. The ambient oxygen is easily adsorbed on the defective $MoTe_2$ surface and leads to significant changes in optical and electrical properties²⁵. We found that the Te/Mo ratio and oxygen content in the as-sputtered film correlated strongly with the phase of SPC $MoTe_2$ and the electrical characteristics of $MoTe_2$ FETs. Furthermore, SPC temperature and time are critical factors for determining the phase of SPC $MoTe_2$. This work provides a complete strategy and experimental database for synthesizing a deterministic $MoTe_2$ phase via SPC and paves a way for novel applications such as integrated circuits, phase-change memory¹⁸, and spintronic devices by exploiting the polymorphic nature of 2D $MoTe_2$.

Results and Discussion

The oxidation effects on the as-sputtered and SPC $MoTe_2$ were first examined using XPS. The amorphous $MoTe_2$ film with a thickness of 5.6 nm was sputtered at 200 °C by using a $MoTe_2$ target, and split into two pieces. One was examined by XPS directly (as-sputtered sample). The other (SPC sample) was immediately transferred to an E-gun evaporation chamber to deposit a 50-nm-thick SiO_2 layer, followed by another 50-nm-thick plasma-enhanced CVD (PECVD) SiO_2 layer. This composite capping layer prevents oxidation and decomposition of $MoTe_2$ in the subsequent SPC process²⁴. The $MoTe_2$ thin film encapsulated in SiO_2 was then annealed in a low-pressure furnace in N_2 to transform into crystalline $MoTe_2$ via SPC. The oxide capping was then removed using a dilute HF solution prior to the XPS analysis. More details about the SPC $MoTe_2$ formation can be found in the Experimental Section. Figure 1 summarizes the SPC synthesis flow and the typical Raman spectra of as-sputtered $MoTe_2$, 2H- $MoTe_2$ (SPC at 650 °C for 24 h) and 1T'- $MoTe_2$ (SPC at 850 °C for 1 h). The characteristic 2H- $MoTe_2$ spectra peak at 171.4 (A_{1g}), 234.7 (E_{2g}^1), and 290.0 (B_{2g}^1) cm^{-1} ; those of 1T'- $MoTe_2$ spectra peak at 163 (B_g), and 262 (A_g) cm^{-1} . The main peaks of 2H- $MoTe_2$ and 1T'- $MoTe_2$ are consistent with those reported in the literature^{2,5,12,24}. Figure 2 shows the measured binding energy spectra of Mo and Te 3d core levels in the as-sputtered and SPC 2H- $MoTe_2$ samples. The core-excitation states of $3d_{5/2}$ and $3d_{3/2}$ were separated by 3.2 eV and 10.4 eV for the Mo and Te valence states, respectively. For the SPC sample (Fig. 2(a)), the binding energy spectra of Mo $3d_{5/2}$ and Te $3d_{5/2}$ peaked at 228.3 eV (blue curve) and 572.9 eV (red curve), respectively. The calculated Te/Mo ratio was approximately 2.13, in good agreement with a nearly stoichiometric $MoTe_2$. For the as-sputtered sample (Fig. 2(b)), the binding energy values of the Mo $3d_{5/2}$ and Te $3d_{5/2}$ peaks were in line with those of SPC. However, the asymmetric deconvolution envelopes of Mo $3d_{5/2}$ (blue curve) and Mo $3d_{3/2}$ (orange curve) were absent in 2H- $MoTe_2$. The similar asymmetric envelopes were previously observed in a mixed composite of Mo–Te with oxidized metal^{26,27} or 1T'- $MoTe_2$ ^{26,28–30}. The oxidation peaks of Mo $3d_{5/2}$ and Te $3d_{5/2}$ were substantial at 232.68 eV (light blue curve) and 576.68 eV (pink curve). By contrast, the Mo–O and Te–O peaks in 2H- $MoTe_2$ were significantly reduced, and this is attributed to the recrystallization of Mo–Te bonds at high temperature. The encapsulated structure contained the Mo and Te atoms from out-diffusion and facilitated Mo–Te bonding during SPC²⁴. To elucidate the origin of oxidation in as-sputtered $MoTe_2$, a much thicker $MoTe_2$ (56 nm thick) was sputtered to investigate its depth profiling of composition via XPS, as shown in Fig. S1. The characteristic oxygen 1s peaks were observed only at the film surface, excluding the possibility of oxygen incorporation during the sputtering deposition. The surface oxidation of the as-sputtered $MoTe_2$ was mainly due to the exposure to ambient air at room temperature. We expect a similar but potentially weaker surface oxidation effect would be

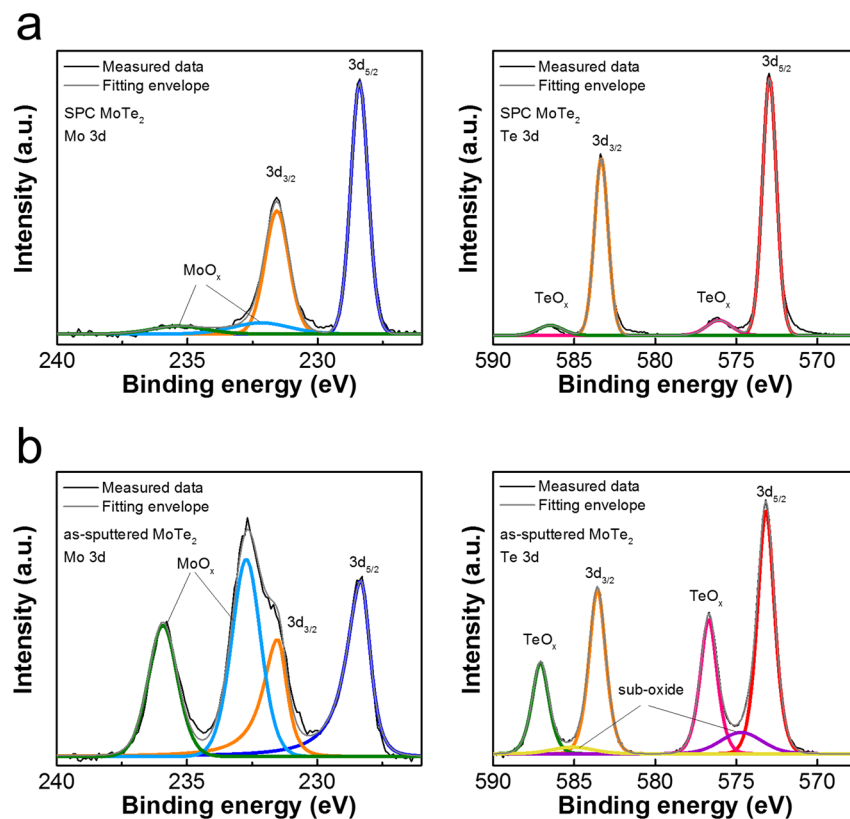


Figure 2. Oxidation effect in MoTe₂. XPS spectra of Mo 3d and Te 3d core levels in (a) SPC crystalline 2H-MoTe₂ and (b) as-sputtered amorphous MoTe₂. The deconvolution fitting was performed to identify distinct binding energy peaks of Mo (3d_{5/2}, 3d_{3/2}), Te (3d_{5/2}, 3d_{3/2}), and their corresponding oxidized states.

unavoidable even when the as-sputtered film is immediately encapsulated by the SiO₂ capping layer because the sample has to be transferred in air between the sputter and evaporator chamber in the present experimental setup.

Substrate heating temperature is known to be an effective knob for engineering the composition, texture, roughness, crystallinity, and nucleation of sputtering films^{31,32} by providing additional migration energy of atoms at the surface. Therefore, we further investigated the SPC effect of MoTe₂ films sputtered at different substrate temperatures from 25 to 500 °C. Figure S2 shows their respective fittings of Raman spectra. Similar to that shown in Fig. 1, the as-sputtered MoTe₂ remained mostly amorphous with no strong characteristic peaks corresponding to crystalline MoTe₂. The weak 1T' characteristic peaks and the asymmetric Mo 3d envelopes shown in Fig. 2(b) suggest possible formation of some 1T' nucleation sites in as-sputtered films. However, the thermal energy provided during sputtering was insufficient to facilitate the recrystallization of MoTe₂. The Raman intensity degraded when sputtered at 500 °C and above, indicating a decomposition of films. On the other hand, XPS spectra of Mo 3d core levels in Fig. 3(a) show that the substrate temperature correlated strongly with the film composition even when the identical sputter target was used. Figure 3(b) shows the deconvolution of XPS spectra designated to the Mo–Te and Mo–O bonds. The intensity of the Mo–O peak decreased with increasing substrate temperature while the change on the Mo–Te peak was relatively small except for the sample sputtered at 500 °C. The inset of Fig. 3(b) shows a similar phenomenon for the XPS spectra of Te 3d core levels. Figure 3(c) shows the ratio of the integrated area between composite states (Mo–Te) and oxidation states (Mo–O, Te–O). The relative areas of Mo–Te gradually increased with temperature. The MoTe₂ films sputtered at high temperatures became more resistant to surface oxidation when exposed to air (inset of Fig. 3(c)). While the exact root cause is still under investigation, two plausible mechanisms are: the bonding strength between Mo and Te is higher or the density of MoTe₂ is higher when sputtered at high temperatures so that the film is more robust against oxidation or oxygen diffusion. Figure 3(d) shows the calculated atomic percentages of O, Mo, and Te atoms. The amount of oxygen decreased from 70 at.% at room temperature to 59 at.% at 500 °C. The ratio of Te/Mo remained at around 1.8 to 2.0 when sputtered at up to 400 °C. The ratio corresponds to the composition of the sputter target. When sputtered at 500 °C, the Te/Mo ratio decreased to 1.4 because of the low sublimation temperature of tellurium^{33,34}. The degree of oxidation also reduced with increasing the film thickness (Fig. S3), i.e. the relative percentage of the oxidized region is less in a thicker film, which supports the surface oxidation effect. The phase of MoTe₂ after SPC depends strongly on the composition of the as-sputtered film. SPC at 650 °C for 24 h was performed on MoTe₂ sputtered at different temperatures and with different thicknesses ranging from 4.5 to 6.5 nm. The final phase diagram confirmed by Raman analysis is summarized in Fig. 4. It is worth noting that different from the previous phase diagram reported for the MoTe₂ bulk crystals synthesized using CVT², the results here consider the effects of 2D SPC in ultrathin films and additional oxygen incorporation. Three distinct regions of 1T', 2H, and mixed 1T'–2H phases were observed.

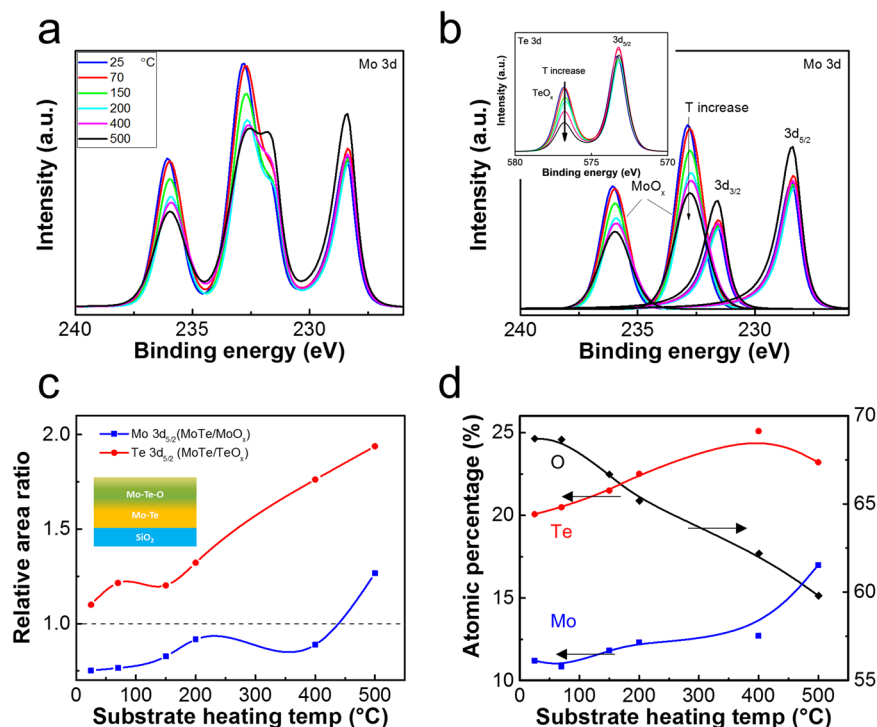


Figure 3. Composition of as-sputtered MoTe₂. XPS spectra of (a) Mo 3d convolution peaks and (b) Mo 3d deconvolution peaks from as-sputtered MoTe₂ films deposited at various temperatures. Inset in (b) shows the corresponding XPS spectra of Te 3d. (c) The ratios of the integrated area calculated from the Mo 3d_{5/2} (~228 eV), Te 3d_{5/2} (~573 eV), MoO_x 3d_{5/2} (232.6 eV), and TeO_x 3d_{5/2} (576.6 eV) deconvolution peaks in (b). The degree of oxidation depends strongly on the substrate heating temperature. (d) Atomic percentages of Mo, Te and O atoms. The amount of oxygen in MoTe₂ decreased with increasing substrate heating temperature while the ratio of Te/Mo remained nearly constant except for that at 500 °C. The reduction of Te/Mo ratio at 500 °C was due to the Te sublimation.

For MoTe₂ sputtered at high temperatures around 500 °C, Te-deficient composition due to Te sublimation stabilized the 1T' phase after SPC². For those sputtered at temperatures below 500 °C, the nearly stoichiometric MoTe₂ composition favored the 2H phase². However, for those sputtered at temperatures below 150 °C, homogeneous 2H-MoTe₂ was difficult to obtain across a large area. A mixture of 1T' and 2H phases was observed. A three-step process for recrystallizing 2H-MoTe₂ was previously reported²⁴. Amorphous as-sputtered MoTe₂ is first crystallized homogeneously into 1T'-MoTe₂. The preferential 1T'-MoTe₂ formation is possibly due to the favorable strain condition in the encapsulated structure¹⁹, abundant local tellurium vacancies in the amorphous film¹², or potential formation of 1T' nucleation sites aforementioned. As the SPC progresses, a few nucleation sites of 2H-MoTe₂ start to develop in localized Te-rich regions. Finally, the entire 1T'-MoTe film is recrystallized into a homogeneous 2H-MoTe₂ phase from the nucleation sites. Therefore, the mixed 1T'-2H phase could be attributed to the retardation of the 2H-MoTe₂ nucleation or recrystallization at the presence of excessive surface oxidation when sputtering MoTe₂ at low temperatures. Thinner MoTe₂ is more prone to both Te sublimation and surface oxidation, and thus the stable 2H-MoTe₂ region in Fig. 4 shrunk substantially as the thickness of MoTe₂ reduced.

To further correlate the relations among composition, SPC growth, and final electrical properties, back-gated transistors were fabricated on the 2H-MoTe₂ samples sputtered at different temperatures. All samples received the same SPC annealing at 650 °C for 24 h. 25-nm Pd metal was used as the source/drain contacts. Figure 5(a) illustrated typical current-voltage transfer characteristics. All the devices exhibited p-type conduction characteristics, but that sputtered at 200 °C presented the strongest p-type conduction and best electrical performance. In Fig. 5(b–f), statistical plots of the major device parameters showed a consistent trend. The field-effect hole mobility μ_h in the linear region was extracted using $\mu_h = (dI_D/dV_G)(L/W)(1/V_D C_G)$ at $V_D = -1$ V where L , W , and C_G represent the channel length, channel width, and gate capacitance per unit area, respectively. The extracted mobility from the device sputtered at 200 °C was comparable with those reported for CVT MoTe₂^{2,6,8}. The non-monotonic dependence of device performance on the sputtering temperature might be related to the oxygen doping effect. Oxygen incorporation is known to induce p-type doping in MoTe₂³⁵. A suitable amount of oxygen introduced by surface oxidation presented a negligible adverse effect of SPC retardation while providing necessary p-type doping. By contrast, the intrinsic MoTe₂ obtained from the CVT method with minimal defects usually exhibits ambipolar conduction^{7,35,36}. Precisely controlling oxygen content in MoTe₂ is critical for enabling p-type conduction even when both the MoTe₂ and SiO₂ capping are deposited in the same chamber with no intentional air exposure in between.

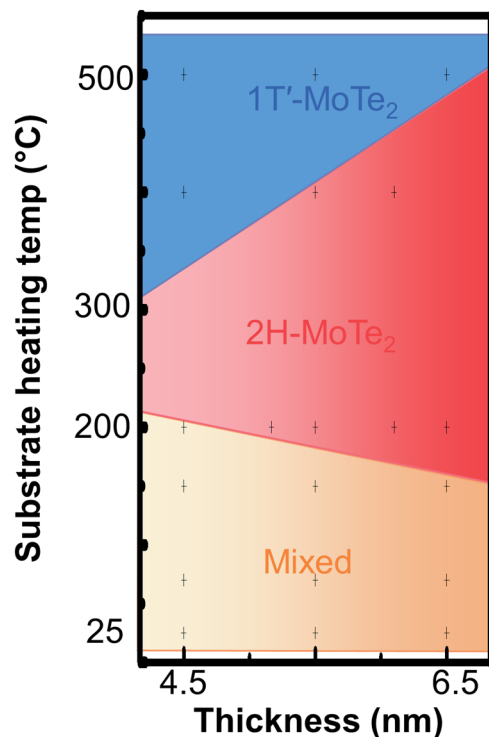


Figure 4. Polymorphic SPC phase diagram as function of substrate heating temperature and thickness of as-sputtered MoTe₂. The SPC was performed at 650 °C for 24 h for all samples. When sputtered at 500 °C, the 1T' phase after SPC is attributed to the Te-deficient composition due to Te sublimation. Below 150 °C, mixtures of 1T' and 2H phases were observed because excessive oxygen might retard the nucleation and recrystallization of 2H-MoTe₂. Homogeneous 2H-MoTe₂ after SPC was obtained between 200 to 400 °C depending on the MoTe₂ thickness.

Figure 6 shows the effect of SPC temperature and dwell time on the polymorphic phase diagram of MoTe₂. The same MoTe₂ sample with a thickness of 6.5 nm sputtered at 200 °C was split into smaller pieces, and then these pieces were subjected to SPC at 500 °C to 850 °C for 1 h to 24 h. Three distinct regions, the 2H phase (red background), 1T' phase (blue background), and amorphous phase (dark blue background), were observed. For a high SPC temperatures at 850 °C, 1T' phase was preferable². For SPC temperatures between 600–700 °C, the aforementioned evolution from the 1T' to 2H phase can be observed with increasing the dwell time. For SPC temperatures below 600 °C but above 500 °C, the thermal energy was insufficient for the nucleation of 2H-MoTe₂, and the MoTe₂ stayed at its 1T' phase. For SPC temperatures at 500 °C and below, the thermal energy was even less, and the recrystallization into either 1T'- or 2H-MoTe₂ was prohibited. Therefore, the MoTe₂ remained at the amorphous phase regardless of the dwell time.

Conclusions

We studied the polymorphic control of MoTe₂ synthesis using 2D SPC. The surface oxidation of as-sputtered MoTe₂ depends strongly on the substrate heating temperature during sputtering. The tradeoff of surface oxidation is present. Excessive oxidation retards the formation of homogeneous 2H-MoTe₂, but an appropriate amount of oxygen doping enhances the p-type doping and thus the device performance. Furthermore, SPC thermal budgets depending on the temperature and time may be exploited for stabilizing a deterministic phase of large-area layered MoTe₂. The 2D SPC technique demonstrates versatile controllability on the MoTe₂ phase and presents new opportunities on researching MoTe₂-based devices.

Experimental Section

MoTe₂ sputtering and SPC. Ultra-high vacuum DC magnetron sputtering system with a base pressure of 10⁻⁸ torr was utilized for depositing MoTe₂ films. The films were sputtered on a SiO₂ substrate (300-nm-thick SiO₂ on Si) using a high-purity MoTe₂ target (99.9% purity; Kojundo Chemical Laboratory), an Ar flow of 20 sccm, a working pressure of 10 mTorr, and DC power of 50 watts. The substrate was heated to various temperatures between 25 to 500 °C using a chuck heater and a ramp rate of 31 °C per minute. For the SPC of MoTe₂, the as-sputtered MoTe₂ sample was unloaded from the sputter chamber and transferred in air immediately to another separate electron-gun evaporator to deposit a 50-nm-thick SiO₂ capping layer by using a source of SiO₂ granules, followed by another 50-nm-thick SiO₂ layer deposited by PECVD using SiH₄ and N₂O as precursors at 300 °C. The composite SiO₂ layer suppresses oxidation and decomposition of MoTe₂ in the subsequent annealing. The evaporated SiO₂ layer prevents potential plasma damage or oxidation on the as-deposited films during PECVD while the PECVD SiO₂ is dense and of favorable quality²⁴. The encapsulated MoTe₂ sample was then annealed

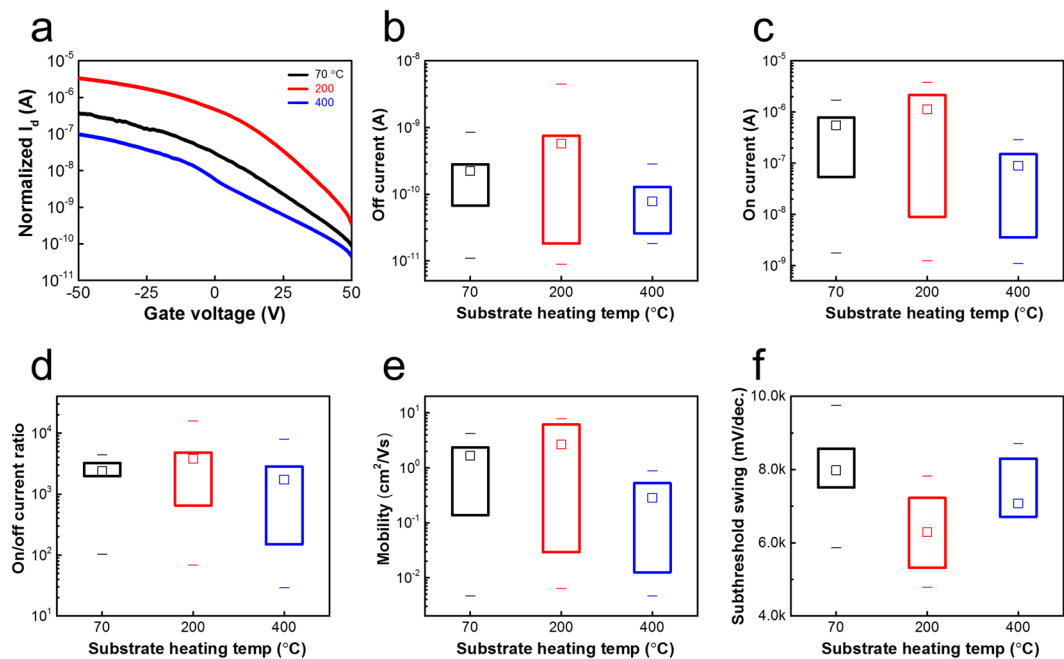


Figure 5. 2H-MoTe₂ back-gated transistor. The SPC layered 2H-MoTe₂ were sputtered at 70, 200 and 400 °C, respectively. (a) Typical current-voltage transfer characteristics. The current was normalized to unit channel length and width. (b–f) Statistical off current, on current, on/off current ratio, mobility, and subthreshold swing of devices, respectively. At least 14 random devices were measured. The channel length (width) ranges from 4(32) μm to 30(100) μm. The measured electrical data were normalized to the unit length and width for fair comparison. The non-monotonic dependence on the sputtering temperature is related to the p-doping effect of oxygen incorporation.

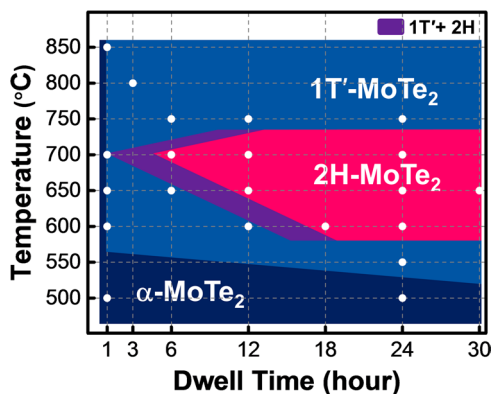


Figure 6. Polymorphic SPC phase diagram as function of SPC temperature and dwell time. The identical 6.5-nm-thick MoTe₂ sputtered at 200 °C was used. 1T' phase was predominant at 850 °C and 500–600 °C. For SPC temperatures between 600–700 °C, the evolution from the 1T' phase to 2H phase was progressed with dwell time. For SPC temperatures at 500 °C and below, the film remained amorphous.

for SPC in a low-pressure furnace at 30 Torr and 650 °C for 24 h in N₂. The SiO₂ capping layer was removed using dilute HF (1.2%) before the XPS analysis of MoTe₂ after SPC.

Properties characterization. Raman spectra were collected in a spectrograph system (Andor Technology; model: SR-500i-D2-R) with a high-performance laser source (Cobolt Samba™, wavelength 532 nm and laser power of 5 mW) and CCD detector (model: DV416A-LDC-DD). The silicon vibration peak located at 520 cm⁻¹ was utilized to calibrate the measurement system. The elemental composition was determined using XPS (Thermo Fisher Scientific Theta Probe, Al Kα X-ray source). The carbon 1 s peak was used to calibrate the reference of binding energy. The measurement was performed in an ultra-high vacuum condition (~10⁻⁹ torr) and with a beam size of 400 μm. For XPS depth profiling, *in-situ* Ar sputtering was utilized with an etching rate of 0.298 nm per second for the as-sputtered MoTe₂ film. The spectra of binding energy were deconvoluted using the Shirley background correction and characterized based on *NIST XPS database*²⁴. The relative sensitivity factors of

Mo 3d_{5/2}, Te 3d_{5/2}, and O 1s were 6.51, 25 and 2.88, respectively. The deconvoluted Mo 3d line shape was fit using an asymmetry distribution of LA (1.1, 2.3, 2) while others were fit using a symmetric distribution of Gaussian–Lorentzian (60).

Fabrication of back-gated transistors. To fabricate back-gated transistors, negative photoresist was spin-coated on the SPC MoTe₂ sample and then baked on a hot plate at 90 °C for 60 s. The contact regions were defined through a mask in a contact aligner using the hard-contact mode and an exposure time of 3 s (light source: NUV, 300 nm–400 nm, 1000 W). After the photoresist development, the sample was baked at 100 °C for 120 s on a hot plate. The SiO₂ capping layer on the contact regions was removed using a dilute HF solution (1.2%). Then, 25-nm-thick Pd metal was deposited using an E-gun evaporator and lifted off in acetone followed by DI water rinse. Finally, the active channel region was defined using the similar photolithography procedure for the contact region and plasma dry etched in Ar + CHF₃ + SF₆. The device characteristics of back-gated FETs were measured at room temperature by using a HP-4156B semiconductor parameter analyzer.

References

- Ruppert, C., Aslan, O. B. & Heinz, T. F. Optical properties and band gap of single- and few-layer MoTe₂ crystals. *Nano Lett.* **14**, 6231–6236, <https://doi.org/10.1021/nl502557g> (2014).
- Keum, D. H. *et al.* Bandgap opening in few-layered monoclinic MoTe₂. *Nat. Phys.* **11**, 482–486, <https://doi.org/10.1038/nphys3314> (2015).
- Zhang, W., Huang, Z., Zhang, W. & Li, Y. Two-dimensional semiconductors with possible high room temperature mobility. *Nano Res.* **7**, 1731–1737, <https://doi.org/10.1007/s12274-014-0532-x> (2014).
- Böker, T. *et al.* Band structure of MoS₂, MoSe₂, and a-MoTe₂: angle-resolved photoelectron spectroscopy and ab initio calculations. *Phys. Rev. B* **64**, 235305, <https://doi.org/10.1103/PhysRevB.64.235305> (2001).
- Zhou, L. *et al.* Large-area synthesis of high-quality uniform few-layer MoTe₂. *J. Am. Chem. Soc.* **137**, 11892–11895, <https://doi.org/10.1021/jacs.5b07452> (2015).
- Cho, S. *et al.* Phase patterning for ohmic homojunction contact in MoTe₂. *Science* **349**, 625–628, <https://doi.org/10.1126/science.aab3175> (2015).
- Nakaharai, S. *et al.* Electrostatically reversible polarity of ambipolar alpha-MoTe₂ transistors. *ACS Nano* **9**, 5976–5983, <https://doi.org/10.1021/acsnano.5b00736> (2015).
- Yin, L. *et al.* Ultrahigh sensitive MoTe₂ phototransistors driven by carrier tunneling. *Appl. Phys. Lett.* **108**, 043503, <https://doi.org/10.1063/1.4941001> (2016).
- MacNeill, D. *et al.* Control of spin–orbit torques through crystal symmetry in WTe₂/ferromagnet bilayers. *Nat. Phys.* **13**, 300–305, <https://doi.org/10.1038/nphys3933> (2016).
- Shao, Q. *et al.* Strong Rashba–Edelstein effect-induced spin–orbit torques in monolayer transition metal dichalcogenide/ferromagnet bilayers. *Nano Lett.* **16**, 7514–7520, <https://doi.org/10.1021/acs.nanolett.6b03300> (2016).
- Duerloo, K.-A. N., Li, Y. & Reed, E. J. Structural phase transitions in two-dimensional Mo- and W-dichalcogenide monolayers. *Nat. Commun.* **5**, 4214, <https://doi.org/10.1038/ncomms5214> (2014).
- Zhou, L. *et al.* Synthesis of high-quality large-area homogenous 1T' MoTe₂ from chemical vapor deposition. *Adv. Mater.* **28**, 9526–9531, <https://doi.org/10.1002/adma.201602687> (2016).
- Park, J. C. *et al.* Phase-engineered synthesis of centimeter-scale 1T' and 2H-molybdenum ditelluride thin films. *ACS Nano* **9**, 6548–6554, <https://doi.org/10.1021/acsnano.5b02511> (2015).
- Empante, T. A. *et al.* Chemical vapor deposition growth of few-layer MoTe₂ in the 2H, 1T', and 1T phases: Tunable properties of MoTe₂ films. *ACS Nano* **11**, 900–905, <https://doi.org/10.1021/acsnano.6b07499> (2017).
- Sun, Y., Wu, S.-C., Ali, M. N., Felsner, C. & Yan, B. Prediction of Weyl semimetal in orthorhombic MoTe₂. *Phys. Rev. B* **92**, <https://doi.org/10.1103/PhysRevB.92.161107> (2015).
- Huang, H. H. *et al.* Controlling phase transition for single-layer MTe₂ (M = Mo and W): Modulation of the potential barrier under strain. *Phys. Chem. Chem. Phys.* **18**, 4086–4094, <https://doi.org/10.1039/c5cp06706e> (2016).
- Ueno, K. & Fukushima, K. Changes in structure and chemical composition of α-MoTe₂ and β-MoTe₂ during heating in vacuum conditions. *Appl. Phys. Express* **8**, 095201, <https://doi.org/10.7567/apex.8.095201> (2015).
- Li, Y., Duerloo, K. A., Wauson, K. & Reed, E. J. Structural semiconductor-to-semimetal phase transition in two-dimensional materials induced by electrostatic gating. *Nat. Commun.* **7**, 10671, <https://doi.org/10.1038/ncomms10671> (2016).
- Song, S. *et al.* Room temperature semiconductor-metal transition of MoTe₂ thin films engineered by strain. *Nano Lett.* **16**, 188–193, <https://doi.org/10.1021/acs.nanolett.5b03481> (2016).
- Sung, J. H. *et al.* Coplanar semiconductor-metal circuitry defined on few-layer MoTe₂ via polymorphic heteroepitaxy. *Nat. Nanotechnol.* **12**, 1064–1070, <https://doi.org/10.1038/nnano.2017.161> (2017).
- Zhou, J. *et al.* Large-area and high-quality 2D transition metal telluride. *Adv. Mater.* **29**, 1603471, <https://doi.org/10.1002/adma.201603471> (2016).
- Yang, L. *et al.* Tellurization velocity-dependent metallic–semiconducting–metallic phase evolution in chemical vapor deposition growth of large-area, few-layer MoTe₂. *ACS Nano* **11**, 1964–1972, <https://doi.org/10.1021/acsnano.6b08109> (2017).
- Wang, S. *et al.* Shape evolution of monolayer MoS₂ crystals grown by chemical vapor deposition. *Chemistry of Materials* **26**, 6371–6379 (2014).
- Huang, J.-H. *et al.* Large-area 2D layered MoTe₂ by physical vapor deposition and solid-phase crystallization in a tellurium-free atmosphere. *Adv. Mater. Interfaces* **4**, 1700157, <https://doi.org/10.1002/admi.201700157> (2017).
- Chen, B. *et al.* Environmental changes in MoTe₂, excitonic dynamics by defects-activated molecular interaction. *ACS Nano* **9**, 5326–5332, <https://doi.org/10.1021/acsnano.5b00985> (2015).
- Wagner, C. *et al.* NIST standard reference database 20, Version 3.4 (Web version). *National Institute of Standards and Technology: Gaithersburg, MD* **20899** (2003).
- Castillo, C. *et al.* Molybdenum trioxide thin films doped with gold nanoparticles grown by a sequential methodology: Photochemical metal-organic deposition (PMOD) and DC-magnetron sputtering. *J. Chil. Chem. Soc.* **61**, 2816–2820 (2016).
- Sacher, E. Asymmetries in transition metal XPS spectra: metal nanoparticle structure, and interaction with the graphene-structured substrate surface. *Langmuir* **26**, 3807–3814, <https://doi.org/10.1021/la902678x> (2010).
- Liu, M. *et al.* Synthesis of few-layer 1T'-MoTe₂ ultrathin nanosheets for high-performance pseudocapacitors. *J. Mater. Chem. A* **5**, 1035–1042, <https://doi.org/10.1039/c6ta08206h> (2017).
- Han, G. H. *et al.* Absorption dichroism of monolayer 1T'-MoTe₂ in visible range. *2D Materials* **3**, 031010, <https://doi.org/10.1088/2053-1583/3/3/031010> (2016).
- Bichsel, R., Buffat, P. & Levy, F. Correlation between process conditions, chemical composition and morphology of MoS₂ films prepared by RF planar magnetron sputtering. *J. Phys. D: Appl. Phys.* **19**, 1575 (1986).
- Depla, D., Mahieu, S. & Greene, J. E. In *Handbook of deposition technologies for films and coatings (Third Edition)* (ed Peter M. Martin) 253–296 (William Andrew Publishing, 2010).

33. Ohsugi, I. J., Tokunaga, D., Kato, M., Yoneda, S. & Isoda, Y. Dissociation and sublimation of tellurium from the thermoelectric tellurides. *Mater. Res. Innov.* **19**, S5-301-S305-303, <https://doi.org/10.1179/1432891714z.0000000001097> (2015).
34. Riley, B. J., Johnson, B. R., Schaefer, H. T. & Sundaram, S. K. Sublimation–condensation of multiscale tellurium structures. *J. Phys. Chem. C* **117**, 10128–10134, <https://doi.org/10.1021/jp400363a> (2013).
35. Qu, D. *et al.* Carrier-type modulation and mobility improvement of thin MoTe₂. *Adv. Mater.* **29**, <https://doi.org/10.1002/adma.201606433> (2017).
36. Lin, Y.-F. *et al.* Ambipolar MoTe₂ transistors and their applications in logic circuits. *Adv. Mater.* **26**, 3263–3269, <https://doi.org/10.1002/adma.201305845> (2014).

Acknowledgements

This work was supported by the Ministry of Science and Technology, Taiwan under grant: 106-2221-E-009-145-MY3 and 107-2633-E-009-003 (Research of Excellence program), the Ministry of Education, Taiwan, the Asian Office of Aerospace Research and Development (AOARD), the Office of Naval Research Global (ONRG), and AU Optronics. The authors thank to the Nano Facility Center at National Chiao Tung University and National Nano Device Laboratories, where the experiments in this paper were performed.

Author Contributions

J.H., H.H., D.W. and W.T. carried out the experiments and analyzed the data. C.C., Y.J. and T.H. design and coordinate the project. J.H. and T.H. wrote the manuscript. All authors discussed the results and contributed to the final manuscript.

Additional Information

Supplementary information accompanies this paper at <https://doi.org/10.1038/s41598-019-45142-x>.

Competing Interests: The authors declare no competing interests.

Publisher's note: Springer Nature remains neutral with regard to jurisdictional claims in published maps and institutional affiliations.



Open Access This article is licensed under a Creative Commons Attribution 4.0 International License, which permits use, sharing, adaptation, distribution and reproduction in any medium or format, as long as you give appropriate credit to the original author(s) and the source, provide a link to the Creative Commons license, and indicate if changes were made. The images or other third party material in this article are included in the article's Creative Commons license, unless indicated otherwise in a credit line to the material. If material is not included in the article's Creative Commons license and your intended use is not permitted by statutory regulation or exceeds the permitted use, you will need to obtain permission directly from the copyright holder. To view a copy of this license, visit <http://creativecommons.org/licenses/by/4.0/>.

© The Author(s) 2019